



# Deactivation analyses of CeO<sub>2</sub>/CuO catalysts in the preferential oxidation of carbon monoxide

Shanghong Zeng<sup>a</sup>, Kewei Liu<sup>a</sup>, Lu Zhang<sup>a</sup>, Bin Qin<sup>b</sup>, Tianjia Chen<sup>a</sup>, Yueling Yin<sup>a</sup>, Haiquan Su<sup>a,\*</sup>

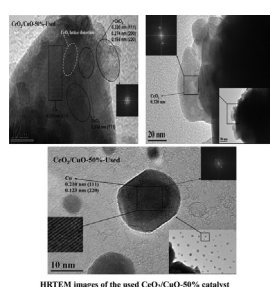
<sup>a</sup> Inner Mongolia Key Laboratory of Chemistry and Physics of Rare Earth Materials, School of Chemistry and Chemical Engineering, Inner Mongolia University, Hohhot 010021, PR China

<sup>b</sup> Petrochina Hohhot Petrochemical Company, Hohhot 010070, PR China

## HIGHLIGHTS

- CeO<sub>2</sub>/CuO-X catalysts were prepared by hydrothermal and impregnation methods.
- CuO microspheres consist of sheet-like CuO and form shell structure.
- CeO<sub>2</sub> particles are supported on CuO microspheres or embedded in pores of CuO.
- Change of CeO<sub>2</sub>/CuO catalyst is another reason for decrease of CO conversion.
- Reduction of CuO and separation of metallic copper from surface of catalyst.

## GRAPHICAL ABSTRACT



## ARTICLE INFO

### Article history:

Received 18 December 2013  
Received in revised form  
11 March 2014  
Accepted 13 March 2014  
Available online 22 March 2014

### Keywords:

Hydrogen  
Cerium–copper catalysts  
Deactivation  
Preferential oxidation of carbon monoxide

## ABSTRACT

The hydrothermal in combination with impregnation methods are used to prepare the CeO<sub>2</sub>/CuO-X catalysts with spherical structure. The catalysts are characterized via SEM, XRD, H<sub>2</sub>-TPR, HRTEM, XPS and N<sub>2</sub> adsorption–desorption techniques. The study shows that the microspheres of CuO consist of the sheet-like CuO and the way of arrangement results in the formation of shell structure. There is a core in the middle of shell structure, which is composed of the nano-sized CuO particles. CeO<sub>2</sub> particles are supported on the surface of the CuO microspheres or embedded in the pores of sheet-like CuO. It is found that there is another reason for the decrease of CO conversion above 155 °C except H<sub>2</sub> competitive oxidation. It is from the change of the CeO<sub>2</sub>/CuO catalyst during CO-PROX reaction including the reduction of CuO and the separation of metallic copper from the surface of catalyst.

© 2014 Elsevier B.V. All rights reserved.

## 1. Introduction

The increase in demand for clean energy has raised the interest toward proton exchange membrane fuel cells (PEMFC) with high

\* Corresponding author. Tel.: +86 471 4995006; fax: +86 471 4992981.  
E-mail addresses: [shanghongzeng001@163.com](mailto:shanghongzeng001@163.com) (S. Zeng), [haiquansu@yahoo.com](mailto:haiquansu@yahoo.com) (H. Su).

efficiency and high power density [1–4]. Hydrogen in combination with PEMFC is a viable energy alternative to fossil fuels for stationary and mobile applications [4,5]. The reforming of hydrocarbons is considered as the most feasible method to produce large amount of hydrogen-rich gasses [6]. Carbon monoxide is a poison for anode of PEMFC and its concentration must be less than 100 ppm in the hydrogen-rich gasses entering the PEMFC [7–10]. Preferential oxidation of CO (CO-PROX) has been recognized as one

of the most cost-effective and straightforward methods to achieve acceptable CO concentration [1–3,5,7,11–13].

CuO/CeO<sub>2</sub> catalysts have shown promising properties for the CO-PROX process and constitute a more interesting alternative to noble metal catalysts from an economical point of view [7,10,14–18]. The high activity of CuO–CeO<sub>2</sub> catalysts is attributed to synergistic interaction of CuO–CeO<sub>2</sub> interfacial sites, which is favorable for the electron changes between Cu<sup>2+</sup>/Cu<sup>+</sup> and Ce<sup>4+</sup>/Ce<sup>3+</sup> [5,12,19–25]. In the CO-PROX reaction, the presence of hydrogen-rich gasses facilitates the formation of Cu<sup>+</sup> species and oxygen vacancy of the CeO<sub>2</sub>, which can supply the active sites for CO adsorption and lattice oxygen for CO oxidation, respectively [6,18,26–28]. However, CuO/CeO<sub>2</sub> catalysts also have drawbacks in the CO-PROX applications including the rapid decrease of CO<sub>2</sub> selectivity above 100 °C, the narrow temperature window of CO total conversion (about 20 °C) and the certain deactivation during the reaction [19]. The appearance of inverse CeO<sub>2</sub>/CuO catalysts opens a new vision and breaks the traditional concept because the inverse CeO<sub>2</sub>/CuO catalysts possess wider temperature window of CO total conversion and higher CO<sub>2</sub> selectivity in comparison with the classical CuO/CeO<sub>2</sub> catalysts [8,29,30]. In the past three years, we devote to the research of inverse CeO<sub>2</sub>/CuO catalysts. It is found that the classical CuO/CeO<sub>2</sub> catalysts show better activity at lower temperature and the inverse CeO<sub>2</sub>/CuO catalysts present higher CO<sub>2</sub> selectivity when the CO conversion reaches 100% [19].

In this work, the CeO<sub>2</sub> nanoparticles were supported on the CuO with self-assembled spherical structure in order to elucidate the effect of CeO<sub>2</sub> content and morphology of the CuO support on catalytic performance in the CeO<sub>2</sub>/CuO system. Furthermore, the difference between the fresh and used CeO<sub>2</sub>/CuO-50% catalysts was studied for exploring the deactivation reason of CeO<sub>2</sub>/CuO catalysts.

## 2. Experimental

### 2.1. Catalyst preparation

The CuO support was prepared by the hydrothermal method. In a typical procedure, the Cu(NO<sub>3</sub>)<sub>2</sub>·3H<sub>2</sub>O, CO(NH<sub>2</sub>)<sub>2</sub> and polyethylene glycol (PEG, Mw = 6000) were orderly dissolved into 100 ml distilled water, and the mixture was vigorously stirred at room temperature for 1 h. Then the mixture was sealed into a stainless steel autoclave with 120 ml capacity Teflon liner and heated for 9 h at 120 °C. After cooling to room temperature naturally, the precipitate was washed with distilled water and absolute ethyl alcohol, respectively. Further, the precipitate was dried at 120 °C for 5 h and calcined at 400 °C for 4 h in the air.

The as-prepared CuO powders was impregnated with Ce(NO<sub>3</sub>)<sub>3</sub> aqueous solution by equal volume impregnation method. After impregnation, the samples were dried at 80 °C for 24 h and calcined at 400 °C for 1 h in the air. The obtained catalysts were denoted as CeO<sub>2</sub>/CuO-X, where X stands for the mass percentage of CeO<sub>2</sub>/(CuO + CeO<sub>2</sub>) weight ratio.

### 2.2. Catalyst characterization

Scanning electron microscopy images of the catalysts were taken on a Hitachi S-4800 scanning electron microscope, using secondary electrons to form the images. The samples were coated with a thin layer of Pt before scanning.

Powder X-ray diffraction patterns were recorded on a PANalytical X'pert PRO diffractometer with Cu K $\alpha$  source ( $\lambda$  = 0.15406 nm) and a power setting of 40 kV and 100 mA in the range of  $2\theta$  between 0° and 80°. The average crystallite sizes were estimated from the line broadening using the Scherrer's equation.

N<sub>2</sub> adsorption–desorption measurements were performed at liquid nitrogen temperature (–196 °C) using a Micromeritics ASAP2020 adsorption apparatus. Before each measurement, the sample was outgassed for 12 h at 200 °C. The surface area and pore size distribution were determined by the Brunauer–Emmett–Teller (BET) and the Barrette–Joynere–Halenda (BJH) methods, respectively.

H<sub>2</sub> temperature-programmed reduction was carried out on a Micromeritics Apparatus (AutoChemII 2920). The reduction gas was 10% H<sub>2</sub>/Ar gas mixture and the flow rate of gas was 50 ml min<sup>–1</sup>. Approximately 30 mg sample was placed on top of some silica wool in a quartz reactor. Before reduction, the sample was pretreated at 200 °C for 1 h in a N<sub>2</sub> stream in order to remove the contaminants, and then cooled to room temperature. The H<sub>2</sub>/Ar mixture was switched on and the sample was heated with a heating rate of 10 °C min<sup>–1</sup>. The reaction was performed from room temperature to 900 °C.

High resolution transmission electron microscope images were carried out using a FEI tecnai F20 instrument. The samples were dispersed into ethanol with ultrasonic treatment for 10 min, and a drop of the suspension was placed on a copper grid for HRTEM observation.

X-ray photoelectron spectroscopy analyses were performed on a Thermo ESCALAB 250XI with monochromatic Al K $\alpha$  radiation (150 W, 1486.6 eV) for the analyses of the core level signals of O 1s, Cu 2p and Ce 3d. The spectra of samples were recorded with the constant pass energy values at 25 eV, using a analysis area of 500  $\mu$ m diameter.

### 2.3. Catalytic performance test

The preferential oxidation of CO in the hydrogen-rich gasses was carried out in a fixed-bed reactor under atmospheric pressure. The 100 mg catalyst diluted with quartz sands was loaded in quartz tubular reactor and a K-type thermocouple was inserted into the catalyst bed to monitor the reaction temperature. The reaction gasses consisted of 1% O<sub>2</sub>, 1% CO, 50% H<sub>2</sub> and N<sub>2</sub> balance. The space velocity was 40,000 ml g<sup>–1</sup> h<sup>–1</sup> and the reaction was operated from 35 °C to 215 °C. The outlet gases were analyzed online with a set of gas chromatograph (GC–2014) equipped with a thermal conductivity detector. 5A molecular sieve column was used to separate CO, O<sub>2</sub> and N<sub>2</sub>. CO<sub>2</sub> was determined by a TDX column. Water was trapped before the gasses entering the GC and CO<sub>2</sub> was absorbed before entering 5A molecular sieve. The conversion of CO (C<sub>CO</sub>) and the selectivity for CO oxidation (S<sub>CO<sub>2</sub></sub>) were calculated according to the following Eqns. (1) and (2), respectively.

$$C_{CO} = ([CO]_{in} - [CO]_{out}) / [CO]_{in} \times 100\% \quad (1)$$

$$S_{CO_2} = 0.5([CO]_{in} - [CO]_{out}) / ([O_2]_{in} - [O_2]_{out}) \times 100\% \quad (2)$$

## 3. Results

### 3.1. Scanning electron microscopy

Fig. 1 shows SEM micrographs of the as-prepared CuO support. It can be seen that the CuO is self-assembled spherical structure and the radius of microspheres is about 5–10  $\mu$ m. The microspheres of CuO consist of the sheet-like CuO. These sheet-like CuO grow together at the one end, and they are emission-like arrangement at the other end. The way of arrangement results in the formation of shell structure. It is found that there is a core in the middle of shell structure after the shell structure is opened, which is composed of the nano-sized CuO particles.

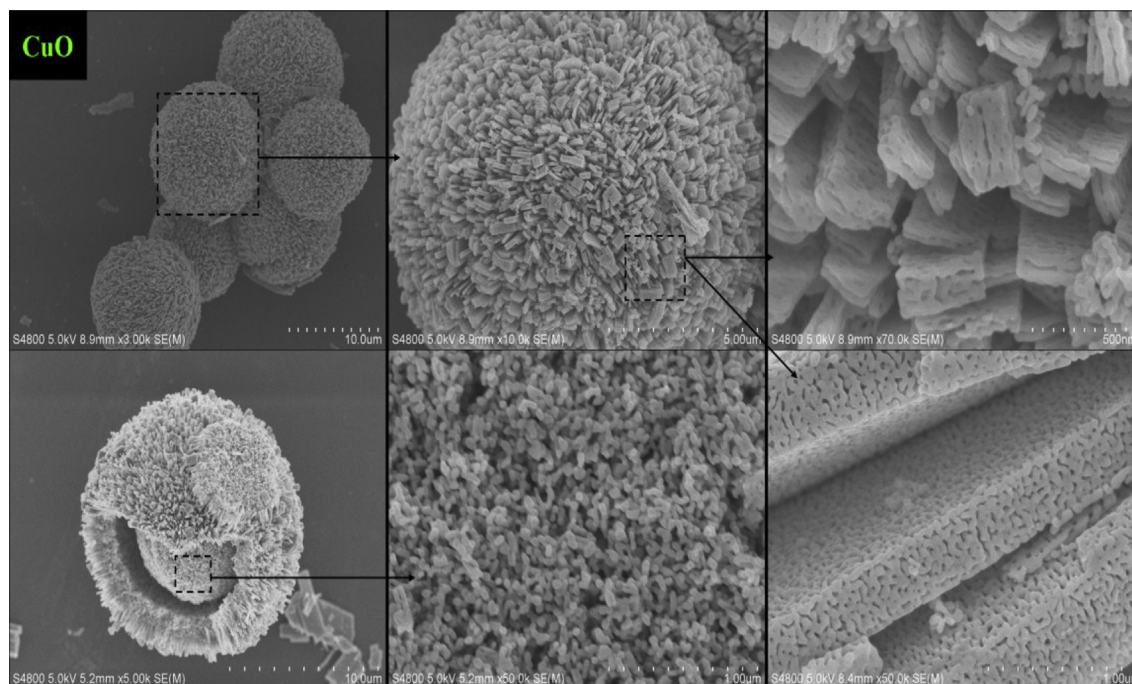


Fig. 1. SEM images of the CuO microspheres.

Fig. 2 shows the SEM micrographs of  $\text{CeO}_2/\text{CuO}$ -20% and  $\text{CeO}_2/\text{CuO}$ -50% catalysts. For  $\text{CeO}_2/\text{CuO}$ -20%, the pores of shell structure become smaller in comparison with the as-prepared CuO, indicating that the  $\text{CeO}_2$  particles are supported on the surface of the CuO microspheres or embedded in the pores of sheet-like CuO. For  $\text{CeO}_2/\text{CuO}$ -50%, the shell structure of CuO is completely covered by the  $\text{CeO}_2$  particles when the content of  $\text{CeO}_2$  increases to 50 wt.%, thus the sheet-like CuO can not be seen in the SEM micrographs.

### 3.2. Structural and textural properties

Fig. 3 shows X-ray diffraction patterns of the  $\text{CeO}_2/\text{CuO}$ -X catalysts. The diffraction peaks of CuO and  $\text{CeO}_2$  were detected in the range of  $2\theta$  between  $10^\circ$  and  $80^\circ$ . The CuO is monoclinic structure in which each Cu atom is bonded to four oxygen atoms. The diffraction peaks of  $\text{CeO}_2$  are assigned to cubic fluorite structure, and the cations of cerium are bonded to eight oxygen neighbors [31]. As can

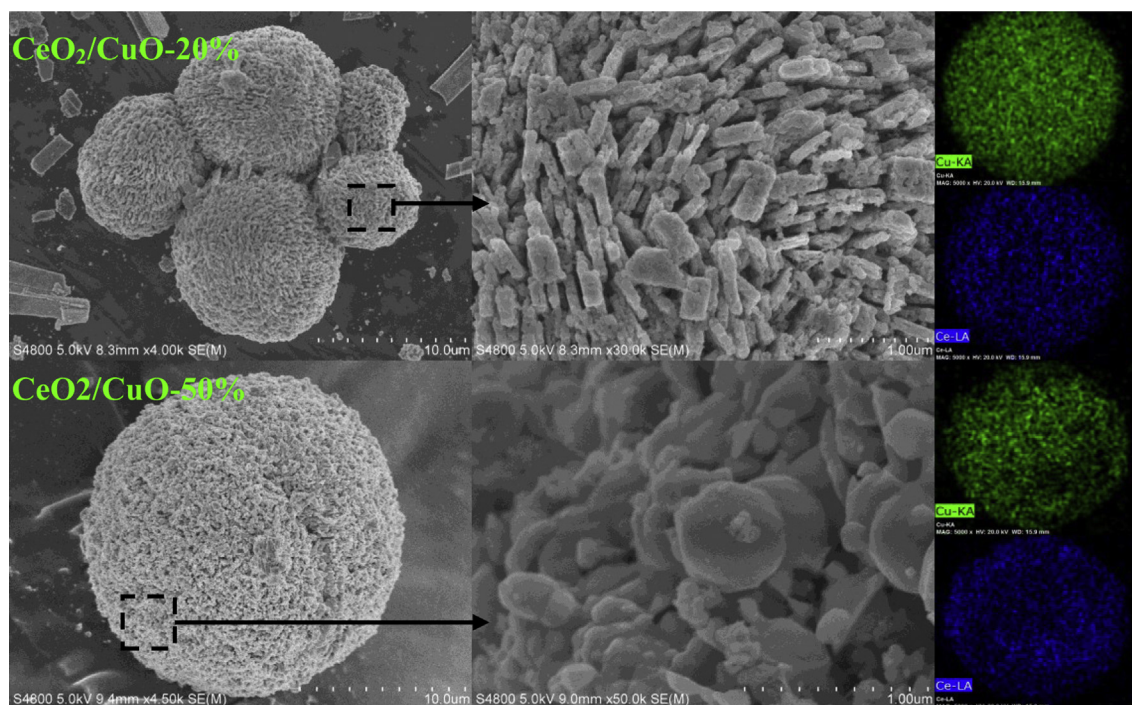


Fig. 2. SEM images of the  $\text{CeO}_2/\text{CuO}$ -20% and  $\text{CeO}_2/\text{CuO}$ -50% catalysts.



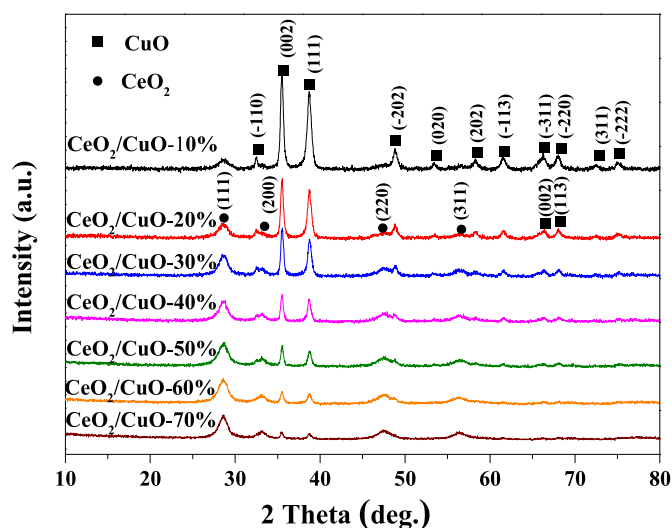


Fig. 3. XRD patterns of the  $\text{CeO}_2/\text{CuO-X}$  catalysts.

be seen in Fig. 3, the diffraction peaks of CuO become weaker and weaker with the increase of  $\text{CeO}_2$  content. Moreover, the diffraction peaks of  $\text{CeO}_2$  are broad, indicating that the  $\text{CeO}_2$  has small crystallite sizes over the  $\text{CeO}_2/\text{CuO-X}$  catalysts.

Table 1 lists the average crystallite sizes of CuO and  $\text{CeO}_2$  calculated from the line broadening of the most intense XRD reflection peaks according to Scherrer's equation. For  $\text{CeO}_2$ , the average crystallite sizes are about 6.0–7.0 nm over the  $\text{CeO}_2/\text{CuO-X}$  catalysts. As shown in SEM measurements, they are dispersed on the surface of the CuO microspheres or embedded in the pores of sheet-like CuO. For CuO, the average crystallite sizes are from 20 to 26 nm, and the self-assembled microspherical structure can promote the dispersion of  $\text{CeO}_2$ . The  $\text{CeO}_2$  with small crystallite size can interact with the bulk CuO on the contact interface [32]. In addition, it can be observed from Table 1 that the cell parameters of  $\text{CeO}_2$  decrease with the increase of  $\text{CeO}_2$  content, which is attributed to  $\text{Cu}^{2+}$  incorporation in the  $\text{CeO}_2$  lattice [12].

Fig. 4 shows  $\text{N}_2$  adsorption–desorption isotherms of the CuO microspheres and  $\text{CuO/CeO}_2\text{-X}$  catalysts. According to five kinds of isotherms from BDDT pore model, they belong to IV-type isotherms, corresponding to typical mesoporous solids [22,33,34]. The pore structure is related to the shape of hysteresis loop on the adsorption–desorption isotherms. The hysteresis loop of CuO is H1 loop, a characteristic of uniform cylindrical pores in the microspherical structure [35]. For the  $\text{CuO/CeO}_2\text{-X}$  catalysts, the hysteresis loops are H2 loops, corresponding to non-ordered worm-like pores due to the incorporation of  $\text{CeO}_2$  in the spherical structure of CuO support [23,36].

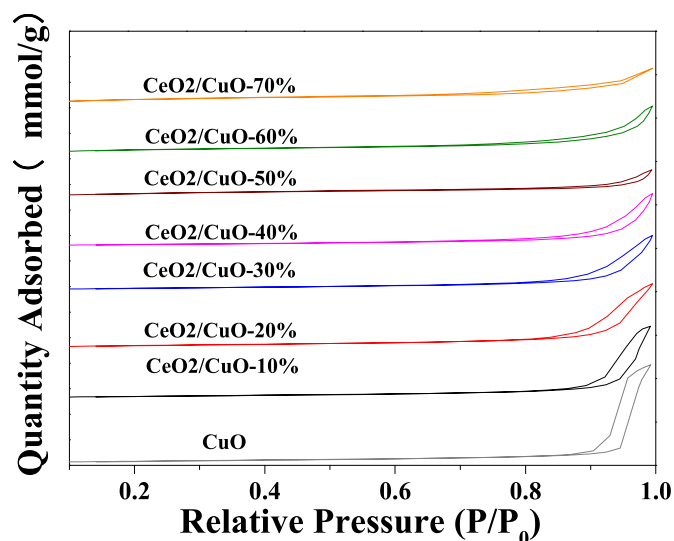


Fig. 4.  $\text{N}_2$  adsorption–desorption isotherms of the CuO microspheres and  $\text{CeO}_2/\text{CuO-X}$  catalysts.

Fig. 5 shows BJH pore size distribution curves of the CuO microspheres and  $\text{CuO/CeO}_2\text{-X}$  catalysts. It can be seen that they display single pore distribution. The most probable peak of the CuO with spherical structure appears at 33 Å, indicating that the CuO microspheres have uniform pores. The most probable peaks of the  $\text{CuO/CeO}_2\text{-X}$  catalysts shift to the direction of small pores with the increase of  $\text{CeO}_2$  content, which further proves that the  $\text{CeO}_2$  particles enter into the pores of the CuO microspheres.

The BET surface area and pore volume of the CuO with spherical structure are  $14.9 \text{ m}^2 \text{ g}^{-1}$  and  $0.152 \text{ cm}^3 \text{ g}^{-1}$ , respectively. As shows in Table 1, the BET surface areas of the  $\text{CuO/CeO}_2\text{-X}$  catalysts increase after  $\text{CeO}_2$  impregnation. However, the pore volume decreases with increasing  $\text{CeO}_2$  content from 10% to 70%, suggesting that one part of  $\text{CeO}_2$  particles are dispersed on the surface of spherical CuO, and another part of  $\text{CeO}_2$  particles occupy in the pores of microsphere-structure CuO.

### 3.3. TPR measurements

Fig. 6 shows  $\text{H}_2$ -TPR profiles of the  $\text{CeO}_2/\text{CuO-X}$  catalysts. For each catalyst, there is one overlapping reduction peak between  $125^\circ\text{C}$  and  $225^\circ\text{C}$  on the  $\text{H}_2$ -TPR profile, which is composed of the reduction peaks of CuO with different particle size. The reduction peak at about  $170^\circ\text{C}$  ( $\alpha$  peak) is assigned to the reduction of small particle CuO, the reduction peak at about  $190^\circ\text{C}$  ( $\beta$  peak)

Table 1  
Structural and textural properties of the  $\text{CeO}_2/\text{CuO-X}$  catalysts.

Sample	$\text{CeO}_2$ (wt.%) <sup>a</sup>	CuO Cell parameter (Å)	$\text{CeO}_2$ Cell parameter (Å)	Particle size(nm) d(CuO) <sup>b</sup> d( $\text{CeO}_2$ ) <sup>c</sup>	$S_{\text{BET}}$ ( $\text{m}^2 \text{ g}^{-1}$ )	Pore volume ( $\text{cm}^3 \text{ g}^{-1}$ )
$\text{CeO}_2/\text{CuO-10\%}$	10.2	4.686 3.427 5.132	5.411	20.1 6.1	14.4	0.112
$\text{CeO}_2/\text{CuO-20\%}$	21.3	4.678 3.428 5.132	5.411	22.5 6.1	19.9	0.103
$\text{CeO}_2/\text{CuO-30\%}$	29.8	4.683 3.426 5.133	5.404	23.2 6.0	15.7	0.087
$\text{CeO}_2/\text{CuO-40\%}$	38.0	4.679 3.426 5.128	5.394	24.8 6.2	14.1	0.084
$\text{CeO}_2/\text{CuO-50\%}$	47.9	4.683 3.435 5.120	5.393	24.9 6.4	32.8	0.046
$\text{CeO}_2/\text{CuO-50\%-Used}$	—	—	5.392	— 6.5	23.7	0.049
$\text{CeO}_2/\text{CuO-60\%}$	61.7	4.681 3.425 5.139	5.393	24.3 6.4	35.4	0.077
$\text{CeO}_2/\text{CuO-70\%}$	69.2	4.685 3.426 5.130	5.386	25.7 7.1	33.2	0.027

<sup>a</sup> Data from the ICP analysis.

<sup>b</sup> Calculated from the Scherrer equation according to the [002] diffraction peaks of CuO.

<sup>c</sup> Calculated from the Scherrer equation according to the [111] diffraction peaks of  $\text{CeO}_2$ .

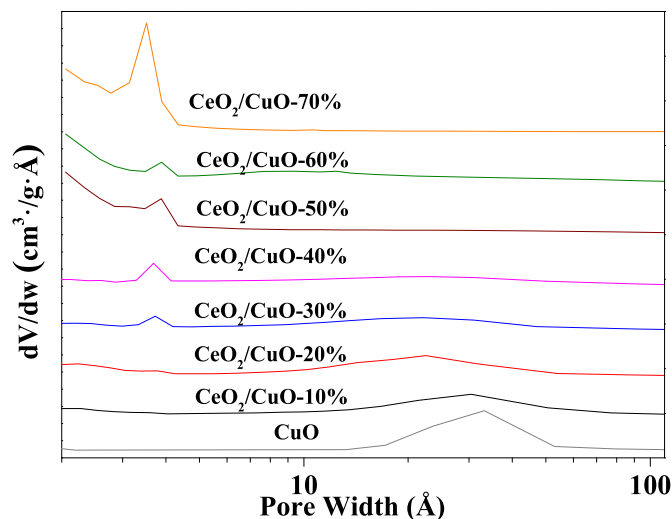


Fig. 5. Pore size distribution curves of the CuO microspheres and CeO<sub>2</sub>/CuO-X catalysts.

corresponds to the reduction of medium size CuO, and the reduction peak at about 200 °C ( $\gamma$  peak) is attributed to the reduction of bulk CuO [2,5,15,22,37–39]. It is obvious that the overlapping reduction peaks become shorter with the increase of CeO<sub>2</sub> content in the CeO<sub>2</sub>/CuO-X catalysts, which can prove that this overlapping reduction peak should be attributed to the reduction of CuO. Compared with the reduction of pure CuO (about 300 °C), the reduction temperature of CuO decreases after CeO<sub>2</sub> impregnation, which is closely associated with the interaction between CeO<sub>2</sub> and CuO [2,3,40,41].

It is reported that pure CeO<sub>2</sub> has the reduction peaks of surface and bulk ceria, which appear at 480 °C and 750 °C, respectively [1,42]. It can be seen from Fig. 6 that the reduction peaks of surface and bulk ceria appear at about 400 °C and 700 °C, and the reduction

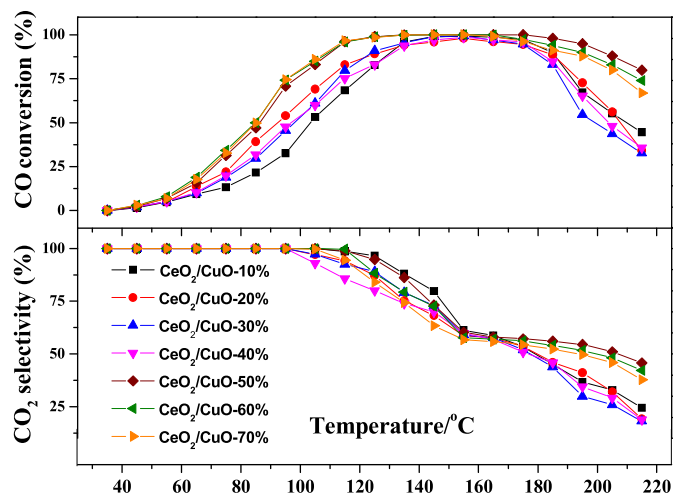


Fig. 7. CO conversion and CO<sub>2</sub> selectivity over the CeO<sub>2</sub>/CuO-X catalysts in the PROX reaction.

peaks shifts to higher temperature with the increase of CeO<sub>2</sub> content. It is obvious that the reduction temperature of CeO<sub>2</sub> decreases after it is supported on the CuO, suggesting that CeO<sub>2</sub> and CuO can promote each other to reduce in the 10% H<sub>2</sub>/Ar gas mixture.

### 3.4. Catalytic performance

Fig. 7 shows CO conversion and CO<sub>2</sub> selectivity over the CeO<sub>2</sub>/CuO-X catalysts in the CO-PROX reaction. The CO-PROX reaction was performed in a gas mixture containing 1% CO, 1% O<sub>2</sub>, 50% H<sub>2</sub> and N<sub>2</sub> balance. It can be seen that all catalysts present a similar catalytic behavior. CO conversion increases with the increase of reaction temperature until the reaction temperature reaches 155 °C. Above 155 °C, CO conversion begins to decrease with the increase of reaction temperature because of H<sub>2</sub> competitive

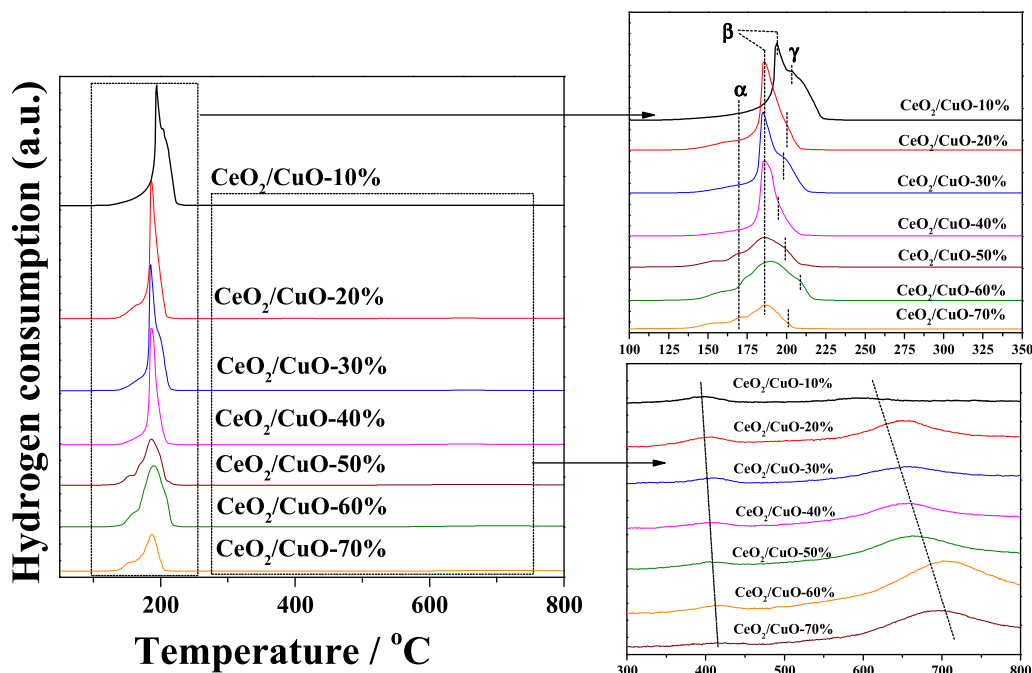


Fig. 6. H<sub>2</sub>-TPR profiles of the CeO<sub>2</sub>/CuO-X catalysts.

oxidation. It is noteworthy that CO conversion and CO<sub>2</sub> selectivity over the CeO<sub>2</sub>/CuO-X catalysts have no great difference when the CeO<sub>2</sub> content varies from 10% to 40%. However, CO conversion and CO<sub>2</sub> selectivity show an obvious promotion when the CeO<sub>2</sub> content increases to above 50%. Among them, the CeO<sub>2</sub>/CuO-50% catalyst presents the best catalytic performance.

### 3.5. Comparison of fresh and used catalysts

#### 3.5.1. XRD and BET comparison

Fig. 8 shows X-ray diffraction patterns of the fresh and used CeO<sub>2</sub>/CuO-50% catalysts. It is obvious that monoclinic CuO and cubic fluorite CeO<sub>2</sub> are present in the fresh CeO<sub>2</sub>/CuO-50% catalyst. After the CO-PROX reaction, the diffraction peaks of CuO become weaker, and the strong peaks of metallic copper were detected in the used CeO<sub>2</sub>/CuO-50% catalyst, indicating that the one part of CuO was reduced into metallic copper in the hydrogen-rich gasses. From Table 1, the average crystallite size of CeO<sub>2</sub> is almost no change over the used CeO<sub>2</sub>/CuO-50% catalyst compared with the fresh catalyst, which suggests that the CeO<sub>2</sub> has no change during the reaction. Furthermore, the BET surface area of the used CeO<sub>2</sub>/CuO-50% catalyst decreases and the pore volume only has minor change after the reaction, indicating that the decrease of BET surface area is closely associated with the reduction of CuO. In other words, the reduction of CuO results in the change of structural and textural properties of the CeO<sub>2</sub>/CuO-50% catalyst during the CO-PROX reaction.

#### 3.5.2. TPR results

Fig. 9 shows H<sub>2</sub>-TPR profiles of the CuO, fresh and used CeO<sub>2</sub>/CuO-50% catalysts. There is one reduction peak at 200 °C in the TPR profile of CuO microspheres, and its shape is sharp and high. The reduction temperature of CuO microspheres decreases compared with the CuO powder reported in the literature [40,41], and it is attributed to the special pore structure of as-prepared CuO which is favorable for gas diffusion. The overlapping reduction peak of CuO still maintains the shape of sharp peak, and the reduction temperature of CuO shifts to lower temperature after loading CeO<sub>2</sub>, which is assigned to the interaction of CeO<sub>2</sub> and CuO on the interface [22]. After the CO-PROX reaction, the overlapping reduction peak of CuO can be seen between 125 °C and 250 °C, however the intensity of peak becomes weaker in comparison with the fresh

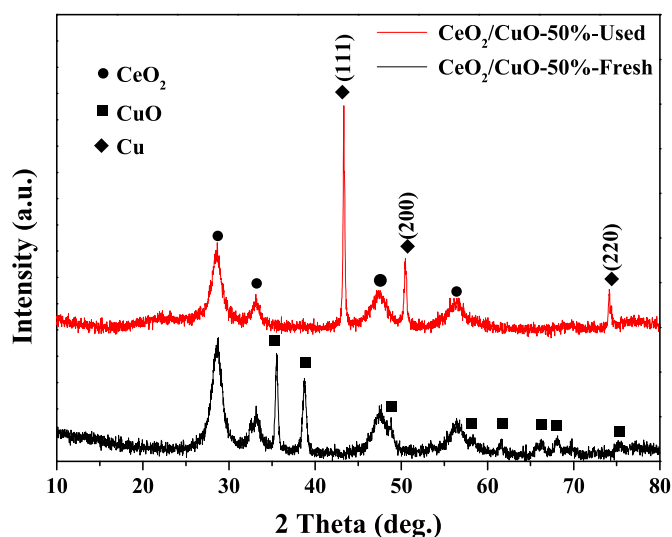


Fig. 8. XRD patterns of the fresh and used CeO<sub>2</sub>/CuO-50% catalysts.

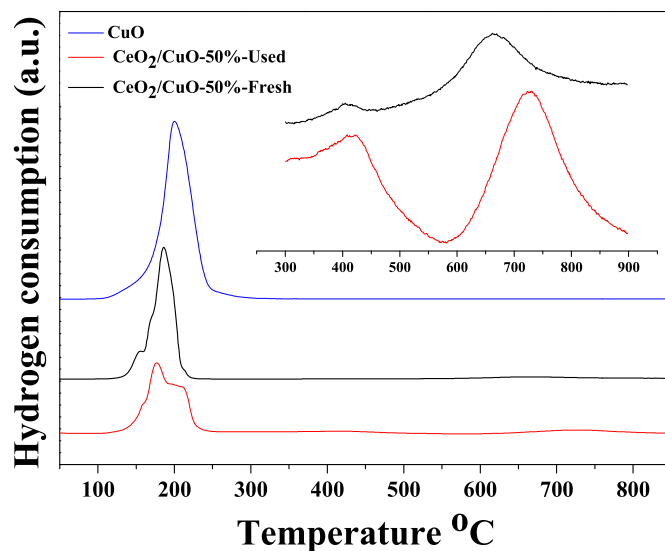


Fig. 9. H<sub>2</sub>-TPR profiles of the CuO microspheres, fresh and used CeO<sub>2</sub>/CuO-50% catalysts.

CeO<sub>2</sub>/CuO-50% catalyst, indicating that one part of CuO was reduced during the CO-PROX reaction. It is consistent with the analyses of 3.5.1 section. As is known, TPR is a highly sensitive detection technique, which can detect trace amounts of substance. Therefore, the CuO with microspherical structure is not completely reduced into metallic copper after the reaction. Namely, the copper exists in the form of metallic copper and CuO in the used CeO<sub>2</sub>/CuO-50% catalyst.

#### 3.5.3. HRTEM analyses

HRTEM measurements were carried out in order to obtain intuitive morphologies of the fresh and used CeO<sub>2</sub>/CuO-50% catalysts. Fig. 10 shows HRTEM images of fresh CeO<sub>2</sub>/CuO-50% catalyst. The particle size of CeO<sub>2</sub> is about 6 nm, and the CeO<sub>2</sub> particles gather into some small clusters, which are dispersed on the CuO microspheres. The contact interface exists between the CeO<sub>2</sub> clusters and the CuO microspheres [43]. Fig. 11 shows HRTEM images of the used CeO<sub>2</sub>/CuO-50% catalyst. After the CO-PROX reaction, the particle size of CeO<sub>2</sub> has no obvious change, and the CeO<sub>2</sub> clusters still are loaded on the surface of the CuO microspheres. The distortion of CeO<sub>2</sub> lattice can be seen from Fig. 11 because of Cu<sup>2+</sup> incorporation in the CeO<sub>2</sub> lattice [42]. It is noteworthy that the surface CuO on the CuO microspheres is reduced into the metallic copper. The particles of metallic copper shed from the surface of the CuO microspheres after reaction. The reduction of the CuO microspheres is carried out from outside to inside. The advantage of inverse CeO<sub>2</sub>/CuO is that it can maintain certain contact interface between CeO<sub>2</sub> and CuO above 155 °C though the CuO is continuously reduced in the hydrogen-rich gasses.

#### 3.5.4. X-ray photoelectron spectroscopy

X-ray photoelectron spectroscopy was used to obtain further information about the valence/oxidation state of the elements and the relative abundance on catalyst surface. Cu 2p and Ce 3d signals of the CeO<sub>2</sub>/CuO-50% catalyst were analyzed before and after the CO-PROX catalytic test in order to study the change of chemical state of copper and cerium.

Fig. 12 shows Cu 2p photoelectron profiles of fresh and used CeO<sub>2</sub>/CuO-50% catalysts. The Cu 2p spectra consist of two sets of peaks, corresponding to Cu 2p<sub>3/2</sub> and Cu 2p<sub>1/2</sub>. The Cu 2p spectrum of the fresh CeO<sub>2</sub>/CuO-50% catalyst presents the principal peak of

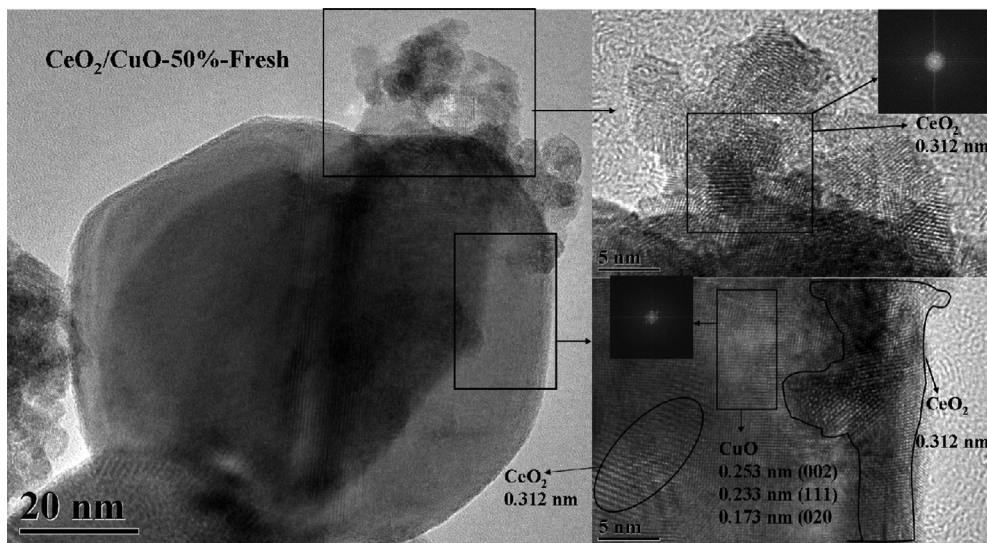


Fig. 10. HRTEM images of the fresh  $\text{CeO}_2/\text{CuO}$ -50% catalyst.

$\text{Cu } 2p_{3/2}$  at about 934.8 eV and the shake-shape satellite peak at 938–948 eV. In addition, it can be seen that a weak  $\text{Cu } 2p_{3/2}$  peak appears at 932.8 eV. For the used  $\text{CeO}_2/\text{CuO}$ -50% catalyst, the  $\text{Cu } 2p_{3/2}$  peak at 931.9 eV becomes stronger and the shake-up peak

becomes weaker. The presence of shake-up peak, a higher  $\text{Cu } 2p_{3/2}$  binding energy (933.0–934.8 eV) and 0.55 intensity ratio of the shake-up satellite to the corresponding principal peak are three major XPS characteristics of  $\text{CuO}$ , while a lower  $\text{Cu } 2p_{3/2}$  binding

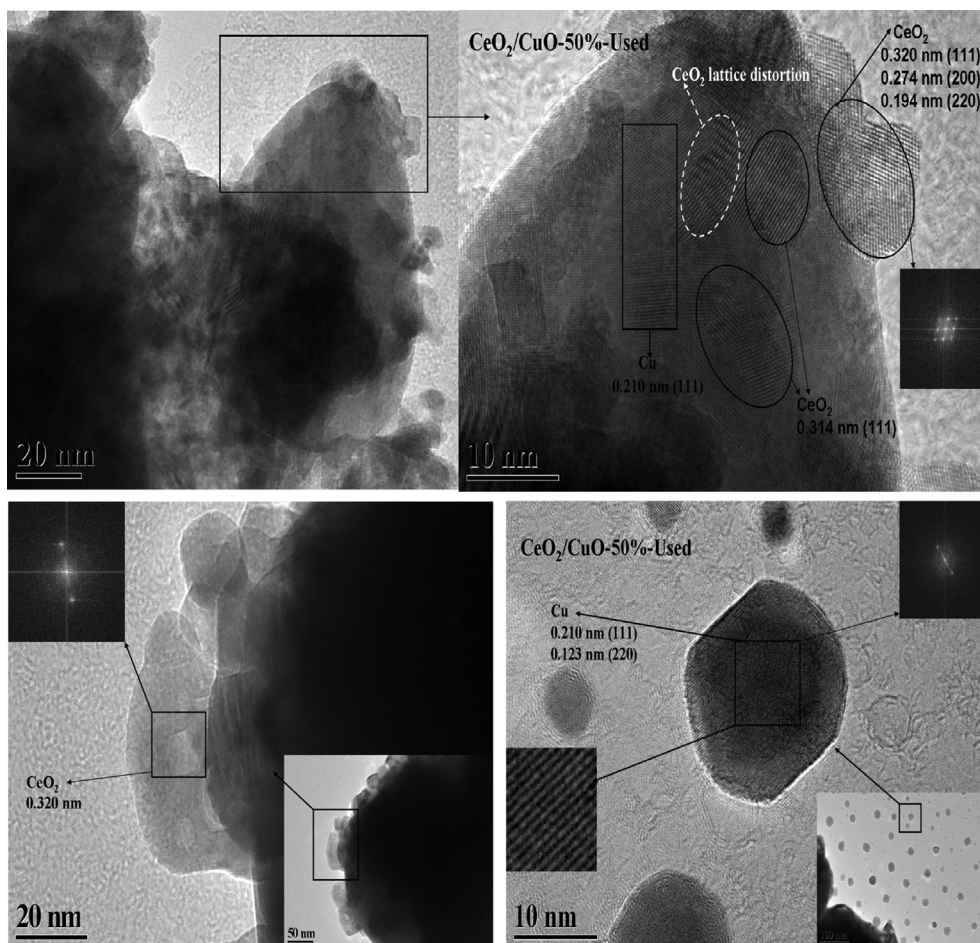


Fig. 11. HRTEM images of the used  $\text{CeO}_2/\text{CuO}$ -50% catalyst.

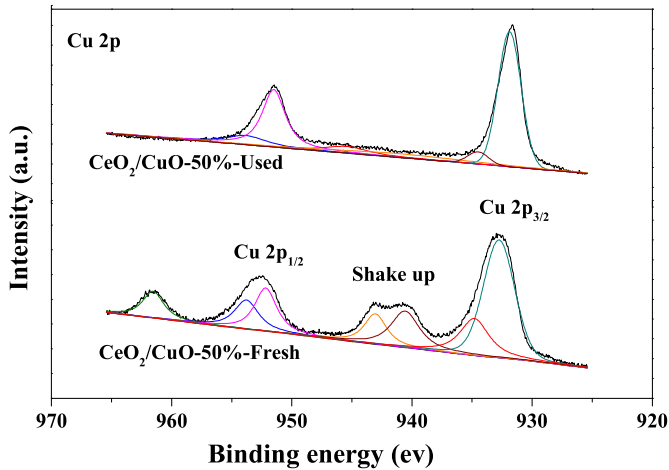


Fig. 12. Cu 2p photoelectron profiles of the fresh and used CeO<sub>2</sub>/CuO-50% catalysts.

energy (931.9–933.1 eV) and the absence of the shake-up peak are characteristics of the reduced copper species [7,20,44,45]. From Table 2, the intensity ratio of the shake-up satellite to the principal peak ( $I_{\text{sat}}/I_{\text{pp}}$ ) is lower than 0.55 for the fresh CeO<sub>2</sub>/CuO-50% catalyst, indicating that copper exists in the form of CuO and the reduced copper species [46,47]. Furthermore, the intensity ratio of the shake-up satellite to the principal peak is 0.12 for the used CeO<sub>2</sub>/CuO-50% catalyst, which suggests that the reduced copper species covers the surface of the catalyst after the reaction.

Fig. 13 shows the core level of Ce 3d signals of the fresh and used CeO<sub>2</sub>/CuO-50% catalysts. It is known that the interpretation of the core level of Ce 3d is not straightforward because of the hybridization between the Ce 4f levels and the O 2p states [31,45]. The complex spectra of Ce 3d signals are composed of eight peaks with the assignment defined in Fig. 13. The two sets of spin-orbital multiplets which are labeled as *u* and *v* correspond to the Ce 3d<sub>3/2</sub> and Ce 3d<sub>5/2</sub> contributions, respectively [7]. It is implied that the Ce<sup>3+</sup> and Ce<sup>4+</sup> are present in the fresh and used CeO<sub>2</sub>/CuO-50% catalysts. The Ce<sup>3+</sup> content is estimated from the following equation when considering the relative area of the  $u_0$  ( $v_0$ ) and  $u'$  ( $v'$ ) peaks to the area of Ce 3d region [7].

$$\begin{aligned} \text{Ce}^{3+}(\%) &= \frac{S(\text{Ce}^{3+})}{S(\text{Ce}^{3+} + \text{Ce}^{4+})} \\ &= \frac{S(u_i) + S(u'_i)}{S(u_i) + S(u'_i) + S(v_i) + S(v'_i)} \times 100\% \end{aligned} \quad (3)$$

Table 2 lists the Ce<sup>3+</sup> content, Ce/Cu preparation ratio and Ce/Cu surface ratio calculated from the XPS measurements. The Ce<sup>3+</sup> content is 16.7% in the fresh CeO<sub>2</sub>/CuO-50% catalyst. After the reaction, the Ce<sup>3+</sup> content increases to 23.2% in the used CeO<sub>2</sub>/CuO-50% catalyst, indicating that the Ce<sup>3+</sup> content increases on the surface during the CO-PROX reaction, which is closely associated

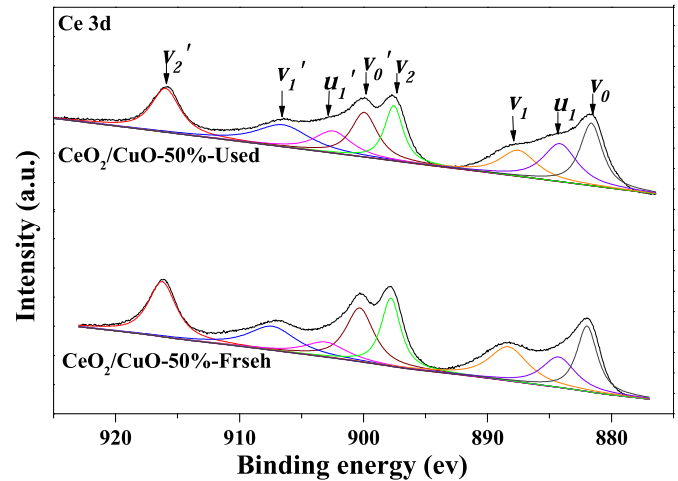


Fig. 13. Ce 3d photoelectron profiles of fresh and used CeO<sub>2</sub>/CuO-50% catalysts.

with the storage and transport of oxygen. Furthermore, the Ce/Cu surface ratio is higher than the Ce/Cu preparation ratio in the fresh CeO<sub>2</sub>/CuO-50% catalyst, which suggests that CeO<sub>2</sub> is dispersed on the surface of the CuO microspheres. It is noteworthy that the Ce/Cu surface ratio increases after the reaction. The possible reason is that the reduced copper species have weak interaction with the CeO<sub>2</sub>, therefore they shed from the surface of catalyst, which is confirmed by the HRTEM measurements.

#### 4. Discussion

It is obvious that the CeO<sub>2</sub> clusters are dispersed on the CuO microspheres over the as-prepared CeO<sub>2</sub>/CuO-*X* catalysts. The contact interface between the CeO<sub>2</sub> clusters and the CuO microspheres can give the active sites for CO oxidation in the reaction. As shown in Fig. 7, CO oxidation occurs above 35 °C, and the reduction of CuO does not begin at this temperature. It indicates that the CuO microspheres can supply the active sites for CO adsorption, and the oxygen vacancy exists in the CeO<sub>2</sub> clusters for provision of lattice oxygen. CO conversion increases with increasing the reaction temperature. It can be seen from Fig. 6 that the reduction of CuO begins at 125 °C. It is possible that the reduction of CuO occurs below 125 °C in the hydrogen-rich gasses because the content of hydrogen in hydrogen-rich gasses is much higher than that in the TPR measurements. It is noteworthy that the occurrence of CuO reduction further improves CO oxidation, which is closely associated with the appearance of monovalent copper ions [8]. The CeO<sub>2</sub>/CuO-*X* catalysts present the best catalytic activity at 155 °C. As mentioned in the section of catalytic performance, CO conversion begins to decrease with the increase of reaction temperature above 155 °C because of H<sub>2</sub> competitive oxidation.

It is possible that there is another reason for the decrease of CO conversion above 155 °C except H<sub>2</sub> competitive oxidation. It is from the change of the CeO<sub>2</sub>/CuO catalyst during CO-PROX reaction. It is

**Table 2**  
Composition and binding energy of the fresh and used CeO<sub>2</sub>/CuO-50% catalysts.

Catalyst	Ce/Cu molar ratio <sup>a</sup>	Ce/Cu Surface ratio <sup>b</sup>	Cu 2p <sub>3/2</sub> BE (eV)	$I_{\text{sat}}/I_{\text{imp}}$	Ce <sup>3+</sup> (%)
CeO <sub>2</sub> /CuO-50%-Fresh	0.46	1.09	934.8 932.8	0.53	16.7
CeO <sub>2</sub> /CuO-50%-Used	0.46	1.21	934.5 931.9	0.12	23.3

<sup>a</sup> Calculated from the preparation condition.

<sup>b</sup> Calculated from the XPS measurements.



obvious that the  $\text{CeO}_2/\text{CuO}$ -50% catalyst has great change after the reaction by comparison of fresh and used  $\text{CeO}_2/\text{CuO}$ -50% catalysts, including the reduction of CuO and the separation of metallic copper from the surface of catalyst. The inverse  $\text{CeO}_2/\text{CuO}$  catalysts possess wider temperature window of CO total conversion and higher  $\text{CO}_2$  selectivity just because they are more difficult to reduce in comparison with the classical CuO/ $\text{CeO}_2$  catalysts due to the presence of bulk CuO.

In a word, there are two reasons, which result in the decrease of CO conversion above 155 °C. One is  $\text{H}_2$  competitive oxidation at higher temperature, and another is the change of the catalyst during the reaction. The solutions have the decrease of reaction temperature or the elevation of reduction temperature of CuO though the reduction of CuO is inevitable.

## 5. Conclusions

The hydrothermal in combination with impregnation methods were used to prepare the  $\text{CeO}_2/\text{CuO}$ -X catalysts. SEM measurements show that the microspheres of CuO consist of the sheet-like CuO and the way of arrangement results in the formation of shell structure. There is a core in the middle of shell structure, which is composed of the nano-sized CuO particles. The analyses of structural and textural properties display that  $\text{CeO}_2$  particles are dispersed on the surface of the CuO microspheres or embedded in the pores of sheet-like CuO. TPR measurements show that  $\text{CeO}_2$  and CuO can promote each other to reduce in the 10%  $\text{H}_2/\text{Ar}$  gas mixture. Catalytic performance tests present that the  $\text{CeO}_2/\text{CuO}$ -50% catalyst has the best catalytic performance. Comparison study of fresh and used catalysts shows that there is another reason for the decrease of CO conversion above 155 °C except  $\text{H}_2$  competitive oxidation. It is from the change of the  $\text{CeO}_2/\text{CuO}$  catalyst during CO-PROX reaction. The solutions have the decrease of reaction temperature or the elevation of reduction temperature of CuO though the reduction of CuO is inevitable.

## Acknowledgments

The authors would like to acknowledge the National Natural Science Foundation of China (grant no. 21066004, 21061008).

## References

- [1] C.G. Maciel, L.P.R. Profeti, E.M. Assaf, J.M. Assaf, J. Power Sources 196 (2011) 747–753.
- [2] Z.W. Wu, H.Q. Zhu, Z.F. Qin, H. Wang, J.F. Ding, L.C. Huang, J.G. Wang, Fuel 104 (2013) 41–45.
- [3] V.D. Araújo, J.D.A. Bellido, M.I.B. Bernardi, J.M. Assaf, E.M. Assaf, Int. J. Hydrogen Energy 37 (2012) 5498–5507.
- [4] Z.K. Zhao, X.L. Lin, R.H. Jin, Y.T. Dai, G.R. Wang, Catal. Sci. Technol. 2 (2012) 554–563.
- [5] F. Mariño, B. Schönbrod, M. Moreno, M. Jobbágy, G. Baronetti, M. Laborde, Catal. Today 133 (2008) 735–742.
- [6] H.B. Zou, S.Z. Chen, Z.L. Liu, W.M. Lin, Powder Technol. 207 (2011) 238–244.
- [7] A. Reyes-Carmona, A. Arango-Díaz, E. Moretti, A. Talon, L. Storaro, M. Lenarda, A. Jiménez-López, E. Rodríguez-Castellón, J. Power Sources 196 (2011) 4382–4387.
- [8] A. Hornés, A.B. Hungria, P. Bera, A.L. Cámara, M. Fernandez-García, A. Martínez-Arias, L. Barrio, M. Estrella, G. Zhou, J.J. Fonseca, J.C. Hanson, J.A. Rodríguez, J. Am. Chem. Soc. 132 (2010) 34–35.
- [9] E.Y. Ko, E.D. Park, H.C. Lee, D. Lee, S. Kim, Angew. Chem. Int. Ed. 46 (2007) 734–737.
- [10] O.H. Laguna, E.M. Ngassa, S. Oraá, A. Álvarez, M.I. Domínguez, F. Romero-Sarria, G. Arzamendi, L.M. Gandía, M.A. Centeno, J.A. Odriozola, Catal. Today 180 (2012) 105–110.
- [11] D. Gamarra, A. Hornés, Z. Koppány, Z. Schay, G. Munuera, J. Soria, A. Martínez-Arias, J. Power Sources 169 (2007) 110–116.
- [12] S.H. Zeng, Y. Wang, K.W. Liu, F.R. Liu, H.Q. Su, Int. J. Hydrogen Energy 37 (2012) 11640–11649.
- [13] E. Moretti, L. Storaro, A. Talon, P. Patrono, F. Pinzari, T. Montanari, G. Ramis, M. Lenarda, Appl. Catal. A Gen. 344 (2008) 165–174.
- [14] W. Liu, M. Flytzani-Stephanopoulos, J. Catal. 153 (1995) 317–332.
- [15] Z.G. Liu, R.X. Zhou, X.M. Zheng, J. Mol. Catal. A Chem. 267 (2007) 137–142.
- [16] G. Avgouropoulos, T. Ioannides, H.K. Matralis, J. Batista, S. Hocevar, Catal. Lett. 73 (2001) 33–40.
- [17] S.M. Ma, G.Z. Lu, Y.X. Shen, Y. Guo, Y.Q. Wang, Y.L. Guo, Catal. Sci. Technol. 1 (2011) 669–674.
- [18] Lj. Kundakovic, M. Flytzani-Stephanopoulos, Appl. Catal. A Gen. 171 (1998) 13–29.
- [19] S.H. Zeng, W.L. Zhang, M. Sliwa, H.Q. Su, Int. J. Hydrogen Energy 38 (2013) 3597–3605.
- [20] L. Qi, Q. Yu, Y. Dai, C.J. Tang, L.J. Liv, H.L. Zhang, F. Gao, L. Dong, Y. Chen, Appl. Catal. B Environ. 119 (2012) 308–320.
- [21] B. Skårman, D. Grandjean, R. Benfield, A. Hinz, A. Andersson, L. Wallenberg, J. Catal. 211 (2002) 119–133.
- [22] M. Luo, J. Ma, J. Lu, Y. Song, Y. Wang, J. Catal. 246 (2007) 52–59.
- [23] S.H. Zeng, W.L. Zhang, N. Liu, H.Q. Su, Catal. Lett. 143 (2013) 1018–1024.
- [24] F. Mariño, C. Descorme, D. Duprez, Appl. Catal. B Environ. 58 (2005) 175–183.
- [25] S.C. Yang, W.N. Su, S.D. Lin, J. Rick, B.J. Hwang, Catal. Sci. Technol. 2 (2012) 807–812.
- [26] C.M. Hung, Powder Technol. 191 (2009) 21–26.
- [27] X.W. Liu, K.B. Zhou, L. Wang, B.Y. Wang, Y.D. Li, J. Am. Chem. Soc. 131 (2009) 3140–3141.
- [28] D.Y. Wang, Y.J. Kang, V. Doan-Nguyen, J. Chen, R. Küngas, N.L. Wieder, K. Bakhmutsky, R.J. Gorte, C.B. Murray, Angew. Chem. Int. Ed. 50 (2011) 4378–4381.
- [29] J.A. Rodríguez, S. Ma, P. Liu, J. Hrbek, J. Evans, M. Pérez, Science 318 (2007) 1757–1760.
- [30] F. Yang, Y. Choi, S. Agnoli, P. Liu, D. Stacchiola, J. Hrbek, J.A. Rodríguez, J. Phys. Chem. C 115 (2011) 23062–23066.
- [31] E. Moretti, L. Storaro, A. Talon, M. Lenarda, P. Riello, R. Frattini, M.D.M. de Yuso, A. Jiménez-López, E. Rodríguez-Castellón, F. Ternero, A. Caballero, J.P. Holgado, Appl. Catal. B Environ. 102 (2011) 627–637.
- [32] A.P. Jia, S.Y. Jiang, J.Q. Lu, M.F. Luo, J. Phys. Chem. C 114 (2010) 21605–21610.
- [33] E. Moretti, M. Lenarda, L. Storaro, A. Talon, T. Montanari, G. Busca, E. Rodríguez-Castellón, A. Jiménez-López, M. Turco, G. Bagnasco, R. Frattini, Appl. Catal. A Gen. 335 (2008) 46–55.
- [34] J. Luo, W. Chu, H. Xu, C. Jiang, T. Zhang, J. Nat. Gas. Chem. 19 (2010) 355–361.
- [35] L.F. Chen, P.J. Guo, L.J. Zhu, M.H. Qiao, W. Shen, H.L. Xu, K.N. Fan, Appl. Catal. A Gen. 356 (2009) 129–136.
- [36] S.F. Zuo, Y.J. Du, F.J. Liu, D. Han, C.Z. Qi, Appl. Catal. A Gen. 451 (2013) 65–70.
- [37] C.G. Maciel, T.D. Silva, M.I. Hirooka, M.N. Belgacem, J.M. Assaf, Fuel 97 (2012) 245–252.
- [38] W.P. Dow, Y.P. Wang, T.J. Huang, Appl. Catal. A Gen. 190 (2000) 25–34.
- [39] L. Dong, Y.H. Hu, F. Xu, D. Lu, B. Xu, Z. Hu, Y. Chen, J. Phys. Chem. B 104 (2000) 78–85.
- [40] Z.G. Liu, R.X. Zhou, X.M. Zheng, J. Mol. Catal. A Chem. 255 (2006) 103–108.
- [41] X.C. Zheng, X.L. Zhang, S.P. Wang, X.Y. Wang, S.H. Wu, J. Nat. Gas. Chem. 16 (2007) 179–185.
- [42] S.H. Zeng, W.L. Zhang, S.L. Guo, H.Q. Su, Catal. Commun. 23 (2012) 62–66.
- [43] Y.J. Kang, X.C. Ye, J. Chen, L. Qi, R.E. Diaz, V. Doan-Nguyen, G.Z. Xing, C.R. Kagan, J. Li, R.J. Gorte, E.A. Stach, C.B. Murray, J. Am. Chem. Soc. 135 (2013) 1499–1505.
- [44] X.D. Ma, X. Feng, X. He, H.W. Guo, L. Lv, J. Guo, H.Q. Cao, T. Zhou, Micropor. Mesopor. Mater. 158 (2012) 214–218.
- [45] E. Moretti, M. Lenarda, P. Riello, L. Storaro, A. Talon, R. Frattini, A. Reyes-Carmona, A. Jiménez-López, E. Rodríguez-Castellón, Appl. Catal. B Environ. 129 (2013) 556–565.
- [46] G. Avgouropoulos, T. Ioannides, Appl. Catal. B Environ. 67 (2006) 1–11.
- [47] H.X. Mai, L.D. Sun, Y.W. Zhang, R. Si, W. Feng, H.P. Zhang, H.C. Liu, C.H. Yan, J. Phys. Chem. B 109 (2005) 24380–24385.